

March 1991

Interim, Aug 90 - Jan 91

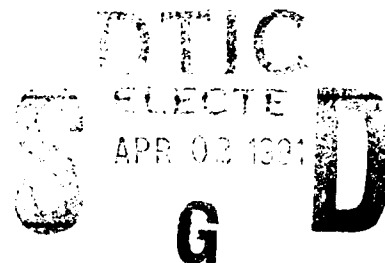
Thin Layer Navier-Stokes Solutions for Transonic Multibody
Interference

PE: 62602F
PR: 2567
TA: 03
WU: 29

Prisca L. Lynch
Magdi H. Rizk

Aerodynamics Branch, Weapon Flight Mechanics Division
Armament Directorate, Wright Laboratory
WL/MNAA
Eglin AFB FL 32542-5434

WL/MN-TR-91-23



Approved for public release; distribution is unlimited.

A thin layer, Navier-Stokes flow solver was used to predict the aerodynamics about interfering bodies. Surface pressure distributions compared very well with available experimental data for freestream Mach numbers between 0.60 and 1.20 at an interbody separation distance of 0.8 diameters. Five separate interference regions were identified which contribute to the total interference force, which was an attractive force for all cases investigated. In general, the level of interference increases with increasing free stream Mach number, and decreases with increasing separation distance.

Thin layer Navier-Stokes
Navier-Stokes
Computational Aerodynamics

Interference Aerodynamics

10

UNCLASSIFIED

UNCLASSIFIED

UNCLASSIFIED

UL

GENERAL INSTRUCTIONS FOR COMPLETING SF 298

The Report Documentation Page (RDP) is used in announcing and cataloging reports. It is important that this information be consistent with the rest of the report, particularly the cover and title page. Instructions for filling in each block of the form follow. It is important to **stay within the lines to meet optical scanning requirements.**

Block 1. Agency Use Only (Leave Blank)

Block 2. Report Date. Full publication date including day, month, and year, if available (e.g. 1 Jan 88). Must cite at least the year.

Block 3. Type of Report and Dates Covered. State whether report is interim, final, etc. If applicable, enter inclusive report dates (e.g. 10 Jun 87 - 30 Jun 88).

Block 4. Title and Subtitle. A title is taken from the part of the report that provides the most meaningful and complete information. When a report is prepared in more than one volume, repeat the primary title, add volume number, and include subtitle for the specific volume. On classified documents enter the title classification in parentheses.

Block 5. Funding Numbers. To include contract and grant numbers; may include program element number(s), project number(s), task number(s), and work unit number(s). Use the following labels:

C - Contract	PR - Project
G - Grant	TA - Task
PE - Program Element	WU - Work Unit Accession No.

Block 6. Author(s). Name(s) of person(s) responsible for writing the report, performing the research, or credited with the content of the report. If editor or compiler, this should follow the name(s).

Block 7. Performing Organization Name(s) and Address(es). Self-explanatory.

Block 8. Performing Organization Report Number. Enter the unique alphanumeric report number(s) assigned by the organization performing the report.

Block 9. Sponsoring/Monitoring Agency Name(s) and Address(es). Self-explanatory.

Block 10. Sponsoring/Monitoring Agency Report Number. (If known)

Block 11. Supplementary Notes. Enter information not included elsewhere such as: Prepared in cooperation with...; Trans. of ..., To be published in When a report is revised, include a statement whether the new report supersedes or supplements the older report.

Block 12a. Distribution/Availability Statement.

Denote public availability or limitation. Cite any availability to the public. Enter additional limitations or special markings in all capitals (e.g. NOFORN, REL, ITAR)

DOD - See DoDD 5230.24, "Distribution Statements on Technical Documents."

DOE - See authorities

NASA - See Handbook NHB 2200.2.

NTIS - Leave blank.

Block 12b. Distribution Code.

DOD - DOD - Leave blank

DOE - DOE - Enter DOE distribution categories from the Standard Distribution for Unclassified Scientific and Technical Reports

NASA - NASA - Leave blank

NTIS - NTIS - Leave blank.

Block 13. Abstract. Include a brief (Maximum 200 words) factual summary of the most significant information contained in the report.

Block 14. Subject Terms. Keywords or phrases identifying major subjects in the report.

Block 15. Number of Pages. Enter the total number of pages.

Block 16. Price Code. Enter appropriate price code (NTIS only).

Blocks 17. - 19. Security Classifications. Self-explanatory. Enter U.S. Security Classification in accordance with U.S. Security Regulations (i.e., UNCLASSIFIED). If form contains classified information, stamp classification on the top and bottom of the page.

Block 20. Limitation of Abstract. This block must be completed to assign a limitation to the abstract. Enter either UL (unlimited) or SAR (same as report). An entry in this block is necessary if the abstract is to be limited. If blank, the abstract is assumed to be unlimited.

PREFACE

This project was conducted in-house by the Computational Fluid Dynamics Section of the Wright Laboratory Armament Directorate, Eglin Air Force Base FL 32542-5434. Capt Prisca Lynch and Dr Magdi Rizk were the researchers who conducted the work. This effort was conducted during the period from August 1990 to January 1991, and presents the interim results of this on-going study.



DI
A1

91 2 066

THIN-LAYER NAVIER-STOKES SOLUTIONS FOR TRANSONIC MULTI-BODY INTERFERENCE

PRISCA L. LYNCH*

Wright Laboratory Armament Directorate, Eglin AFB, Florida

MAGDI H. RIZK†

Sverdrup Technology, Inc., Eglin AFB, Florida

ABSTRACT

A thin-layer, Navier-Stokes flow solver was used to predict the aerodynamics about interfering bodies. Surface pressure distributions compared very well with available experimental data for freestream Mach numbers between 0.60 and 1.20 at an interbody separation distance of 0.8 diameters. Five separate interference regions were identified which contribute to the total interference force, which was an attractive force for all cases investigated. In general, the level of interference increases with increasing free stream Mach number, and decreases with increasing separation distance.

INTRODUCTION

The aerodynamic properties and the performance qualities of fighter aircraft are influenced by the aerodynamic forces generated by mutually interfering stores in external carriage. In addition, a knowledge of these forces is necessary for determining the trajectories of these bodies, relative to each other and relative to the aircraft, as they are released.

Experimental and computational investigations of the aerodynamics of mutually interfering bodies have been performed for single, double and triple combinations, Refs [1,2]. In these investigations, Euler solutions were obtained and compared with the experimental measurements.

In the present work, viscous flow solutions are obtained to investigate the aerodynamics of mutually interfering bodies. A main element of the study is the investigation of the forces imposed on the bodies when they are in close proximity. Previous studies were performed for a fixed distance between body centerlines. Each of the studies considered a range of subsonic and supersonic free-stream Mach numbers. The study in Ref [2] showed that the finned bodies tend to be pulled together at subsonic free-stream conditions and to be repulsed at supersonic free-stream conditions. However, the repulsive forces were relatively

weak in comparison to the attractive forces. The importance of viscous effects increases in determining the interactive forces between the bodies as the distance decreases between them. The use of the viscous solver allows us to investigate the interactive forces acting on the bodies at different conditions for which the use of the inviscid solver would not be valid.

GRID GENERATION

The body configuration is a generic store with a cylindrical centerbody, and a tangent ogive forebody and afterbody. The afterbody is truncated to mount to a sting. The radius of the cylindrical centerbody is one inch and the total length of the store is 11.882 inches from the nose to the truncation point at the sting. The tangent ogive forebody and afterbody are given by circular arcs with radius of 6.056 inches. The computational grid for these configurations was generated by the Program EAGLE-Numerical Grid Generation system, Ref [3]. The grid generated for the two and three store configurations is an elliptic, five block, O-C-H grid system. The grid is a single ogive-cylinder-ogive with sting and utilizes two reflection planes to simulate both the two store and three store conditions.

A block structure was chosen which could be easily modified to change the separation distance between the stores. The block structure is basically the same for the two and three store configurations. A cross-sectional cut of the grid, at a constant I plane, is shown for the two store configuration in Figure 1(a), and the three store configuration in Figure 1(b). Blocks 1 and 3 are embedded C grids which surround the store and sting. The C configuration was chosen to maintain orthogonality of grid lines off the nose of the ogive forebody. For these two blocks, the I lines of the computational grid run longitudinally, along the body surface, the J lines are normal to the surface, and the K lines are circumferential about the body. Blocks 2 and 4 are immediately in front of blocks 1 and 3. The I lines in blocks 2 and 4 run longitudinally, along the stagnation line out the nose of the body, J lines are normal to the stagnation line, and K lines are circumferential about the stagnation line. Transition is made from the constant I planes of blocks 1 and 3 to the constant J planes of blocks 2 and 4. This is more easily seen in Figure 1(c), which shows

*Research Engineer, Computational Fluid Dynamics Section, Aerodynamics Branch, Weapon Flight Vehicles Division. Member AIAA.

†Associate Principal Engineer, Aeromechanics Department, TEAS Group. Member AIAA.

This paper is declared a work of the U.S. Government and is not subject to copyright protection in the United States.

a constant K plane cut through the grids. Block 5 transitions the inner blocks 1 and 2, along the reflection planes, to the farfield boundaries. The I lines are longitudinal, J lines are normal, and K lines are circumferential. Blocks 3 and 4 are constrained by the reflection planes and, therefore, require no transition to farfield boundaries.

The reflection planes were aligned along the planes of symmetry for each of the configurations. The included angle between the two reflection planes of the two store configuration is 90 degrees, while that of the three store configuration is 60 degrees. For purposes of analysis, the angle θ is defined as positive clockwise, with $\theta = 0$ starting at the inboard, constrained flow location, to $\theta = \pi$ at the outboard, unconstrained flow location. This is shown in Figure 1(a) for the two store case and Figure 1(b) for the three store case.

The store has 97 points distributed in the streamwise direction with concentration of the surface points at the expected areas of aerodynamic interest, the ogive nose, the shoulder transition to the cylindrical midsection, and the ogive boattail. Additionally, the 32 points in the normal direction (J) were concentrated close to the body surface and smoothly transitioned to the outer boundaries. The total dimensions for blocks 1 and 3 are $97 \times 32 \times 16$ and $97 \times 32 \times 6$, for a total of 21 circumferential points. Dimensions of the remaining blocks were $20 \times 20 \times 16$ for block 2, $20 \times 20 \times 6$ for block 4, and $116 \times 30 \times 16$ for block 5.

FLOW SOLVER

The solutions were obtained using a thin-layer, Navier-Stokes solver based upon that of Ref [4]. The solver uses a flux-difference split scheme based on Roe's approximate Riemann solver. The governing equations are written in strong conservation law form to capture shock waves in the flow field. A finite volume formulation is used to discretize the flow governing equations. The solver uses an implicit, two-pass scheme. Local time-stepping is used to accelerate the convergence of the solution. Characteristic variable boundary conditions are used at the farfield boundaries and no-slip boundary conditions are used at the body surfaces. A multi-block, body conforming computation mesh is used in the computations. Turbulence is modeled by using the Baldwin-Lomax model.

RESULTS

Computations were performed for the flow about interfering bodies at different free stream Mach numbers, M_∞ , and separation distances D , where D is the distance between the bodies at their closest points. A Reynold's number of 1.2×10^6 was chosen, so that the quality of computational results obtained could be measured against the available experimental data of Ref [5]. Extensive comparisons were

made for the varying values of M_∞ and circumferential body locations at $D = 1.6$ inches. Figures 2(a), (b), and (c) show a comparison of pressure coefficient along the surface for the two body configuration at $D = 1.6$ inches, $M_\infty = 0.95$. The pressure distribution for the most constrained flow, the inboard location $\theta = 0$, is shown in Figure 2(a). Computational predictions agree very well with the experimental results through both the expansions at the nose and boattail, and quite accurately predicts the shock location and strength of compression at mid-body. A slight deviation in the prediction of the minimum C_p is noted. Pressure distributions at $\theta = \frac{\pi}{2}$ and $\theta = \pi$ are shown in Figures 2(b) and (c), respectively. In general, the computational predictions agree well with a slight underprediction of the shock strength and recompression. A random selection of experimental comparisons for the two body case at $M_\infty = 0.6, 0.85, 1.05$, and 1.2 are shown in Figures 3(a), (b), (c), and (d). Again, the predicted C_p values agree quite well with experiment for these cases. It should be noted, however, that for the $M_\infty = 0.85$ case the shock location is predicted slightly forward of the experimental result, and the strength of compression is underpredicted. To some extent, this deviation can be attributed to insufficient mesh concentration in this area.

Interference-free flows, for the case of a single body, are axisymmetric. The introduction of a neighboring body results in flow conditions which are different in the unconstrained flow region neighboring the $\theta = \pi$ plane and the constrained flow region neighboring the $\theta = 0$ plane. This destroys the flow axisymmetry. Therefore, the deviation of the flow from symmetry about the xy plane and the deviation of the flow from axisymmetry are measures of flow interference. Examples of parameters which may be used as measures for flow interference are σ_1 , σ_2 and λ . The parameter σ_1 is based on comparing the flow properties along the body at the minimum interference station, $\theta = \pi$, and the maximum interference station, $\theta = 0$. It is given by

$$\sigma_1 = \frac{\int |\Delta C_p(x, 0)| dx}{\pi \frac{d}{2}}$$

where $\Delta C_p(x, 0)$, $\Delta C_p(x, 0) = C_p(x, \pi) - C_p(x, 0)$, is the difference between pressure coefficient distributions at the inboard station, $\theta = 0$, and the outboard station, $\theta = \pi$. The integral is taken over the body length and d is the body diameter. The $\frac{\pi}{2}$ factor appearing in the definition of σ_1 is simply a scaling factor to allow comparisons between σ_1 and σ_2 , which is defined below. Although the parameter σ_1 takes into account the flow properties at only two angular stations, $\theta = 0$, and $\theta = \pi$, it is a indication of interference over the total surface, since the flow along all angular positions is dependent on the conditions at $\theta = 0$ and $\theta = \pi$. The parameter σ_2 is obtained by integrating

the absolute value of $\Delta C_p(x, \theta)$ over the surface area projected onto the xy plane for $-\frac{\pi}{2} \leq \theta \leq \frac{\pi}{2}$, where, $\Delta C_p(x, \theta) = C_p(x, \pi - \theta) - C_p(x, \theta)$. Therefore,

$$\sigma_2 = \frac{\int |\Delta C_p(x, \theta) \hat{e}_z \cdot \hat{n}| dS}{\pi \left(\frac{d}{2}\right)^2}$$

where \hat{e}_z and \hat{n} are the unit vector in the z direction and the unit outward normal to the body surface, respectively, and the integral is taken over the body surface. The parameter λ is based on measuring the flow deviation from axisymmetry. It is given by

$$\lambda = \frac{\int |\Delta f| dS}{S}$$

where S is the body surface area, and $\Delta f = f_i - f_o$, where f is some flow property. Subscript i refers to the interference flow, while subscript o refers to a reference flow distribution which may, for example, be chosen to be that of an interference-free flow (single body), or some average distribution obtained from the interference flow such as

$$f_o(x) = \frac{\int_0^{2\pi} f_i(x, \theta) d\theta}{2\pi}$$

The values of the different parameters suggested above are not expected to be equal, however, the use of any one of them allows a measure of interference to be obtained for comparing the flow at different conditions. The parameters σ_1 and σ_2 are used in the present study. The parameter λ , however, is just given as an additional example for possible interference parameters.

The interference force coefficient, C_A , acting on a body due to a neighboring body is obtained by integrating $\Delta C_p(x, \theta)$ over the surface area projected onto the xy plane for $-\frac{\pi}{2} \leq \theta \leq \frac{\pi}{2}$. Positive ΔC_p values contribute to an attractive interference force, while negative ΔC_p values contribute to a repulsive interference force. Comparisons were made along the body between pressure distributions at $\theta = 0$ and $\theta = \pi$. This resulted in identifying distinct regions along the body where attractive or repulsive interference forces act. It is possible to identify these regions on the basis of comparisons at the $\theta = 0$ and $\theta = \pi$ angular positions, since pressure integrals at these positions are the most highly weighted among all angular positions when computing aerodynamic interference forces and since the flow in the θ direction is generally continuous and gradual variations in flow properties take place as θ varies between the stations $\theta = 0$ and $\theta = \pi$. The total effect, whether repulsive or attractive, depends on the integral effects of all regions.

As the flow moves along the body, it passes through regions of expansion, compression, expansion, and compression, respectively. For a given separation distance, D , the extent of each of these regions

along the body depends on the free-stream Mach number, M_∞ . The upstream and downstream boundary positions for each of these regions are functions of the angle θ , due to the different flow conditions existing in the unconstrained flow region neighboring the $\theta = \pi$ plane and the constrained flow region neighboring the $\theta = 0$ plane. These different flow conditions also cause the strength of the expansions and compressions to depend on θ .

Figure 4(a) compares the pressure distribution along the inboard body stations at $\theta = 0$ (curve *i*) and the outboard body stations at $\theta = \pi$ (curve *o*) for the two body case at $M_\infty = 0.95$ and $D = 1.6$ inches. The nose expansion region, shown in the figure depends on M_∞ . At relatively low M_∞ values, it ends upstream of the front shoulder. The downstream boundary of this region moves toward the shoulder as the free-stream Mach number increases. For all M_∞ values considered here, this region does not extend beyond the shoulder in the unconstrained outboard position, $\theta = \pi$. However, in the constrained, inboard position, $\theta = 0$, it continues to extend further beyond the shoulder as M_∞ continues to increase. The x position of the downstream boundary of the expansion region is generally a decreasing function of θ . The pressure in this region is higher in the inboard side than the outboard side. Due to the relatively early termination of this region in the outboard side, a cross over between curves *i* and *o* occurs at point *B*. The region extending between points *A* and *B* is the front repulsive, *FR*, region. Downstream of point *B*, the flow continues to expand in the inboard side and this expansion is finally terminated by a relatively strong shock. In the outboard side, the flow goes through a compression region terminated by a relatively weak shock. The shock surface terminating the compression region moves downstream as M_∞ increases. However, it moves at a faster rate in the outboard position than at the inboard position. Therefore, a second cross over point occurs at point *C*, creating a center front attractive, *CFA*, region between points *B* and *C*. As the flow continues to compress beyond point *C*, then expand and compress, a center repulsive, *CR*, region between points *C* and *D*, a center back attractive, *CBA*, region between points *D* and *E*, and a back repulsive, *BR*, region between points *E* and *F* are formed. In general, large interference forces associated with the individual regions indicate large flow interference, however, the combined effects of the different regions is not necessarily proportionate to the effects of the individual regions.

The extents and effects of the five regions identified above are strongly dependent on M_∞ . Under certain conditions, some of these regions may be absent. Figure 4(b) compares the inboard pressure distribution (curve *i*) and the outboard pressure distribution (curve *o*) for the two body case at $M_\infty = 0.60$ and

$D = 1.6$ inches. At this low M_∞ value, the flow is nearly axisymmetric and deviations between curves i and o are small. Also, the flow is shockless. The FR region is apparent in this figure, however, the interference effects are not sufficiently strong to cause the front outboard compression region to extend downstream of the front inboard compression region. As a result, the CR region is not formed, and the CFA and CBA regions combine to form a single region. Figure 4(c) compares the pressure distributions at the inboard and outboard stations for $M_\infty = 1.2$. Comparing this figure to Figure 4(a), it is apparent that regions CFA and CR are further expanded as M_∞ increases, while the BR region is completely eliminated.

The pressure comparisons corresponding to the M_∞ values for Figures 4(a), (b), and (c) are shown in Figures 5(a), (b), and (c), for $D = 0.8$ inches. The force regions are apparent in these figures. The reduced separation distance affects the pressure distribution both at the inboard and outboard stations, however, the strongest effects are apparent at the inboard stations, where higher pressure gradients are observed.

Figure 6(a) compares the pressure distributions of the two body case at $M_\infty = 0.95$ for the three separation distances $D = 0.8, 1.2$, and 1.6 inches at $\psi = 0$. A similar comparison is made in Figure 6(b) at $\theta = \pi$. It is clear from Figure 6(a) that a reduced separation distance causes the flow to reach lower pressure levels in the nose expansion region, which is terminated with a stronger shock than the corresponding shock at larger D values, and which is positioned upstream of those in the larger D cases.

Figure 7 compares σ_1 and σ_2 for the 1.6 inch separation distance, while a similar comparison is presented in Figure 8 for the 0.8 inch separation distance. It is clear that both parameters predict the same trends in interference variations with M_∞ . For the large separation distance, $D = 1.6$ inches, it is observed that the level of interference increases with M_∞ , for the range of values considered here. However, the rate of increase in interference levels with M_∞ declines at the larger M_∞ values. At the smaller separation distance, $D = 0.8$ inches, the level of interference increases with M_∞ , until the flow becomes supersonic. Beyond that point the interference levels off and further increases in M_∞ cause it to decline slightly.

Figure 9 shows the variation of the two body interference force with free stream Mach number, for the two separation distances considered here. For the M_∞ range considered, the interference force is an attractive force. For a given M_∞ value, the attractive force increases with reduced distance. For low M_∞ values, the magnitude of the force increases with M_∞ until it reaches its maximum value, at a free stream Mach number of approximately 0.8 . Beyond

that point the attractive force is reduced with increased M_∞ , except for the local maximum at about a M_∞ value of 1.05 . Computations for the separation distance of 1.2 inches were limited to the M_∞ value of 0.95 . The value of C_A for this case is 0.069 , which, as expected, falls between the corresponding values of 0.081 and 0.056 for the $D = 0.8$ inch and $D = 1.6$ inch separation distances, respectively.

Figure 10 compares the relation between C_A and M_∞ , obtained computationally, to the corresponding relation obtained from experimental data. Force measurements were not performed in the experiments described in Ref [5]. The pressure data measurements, however, were integrated numerically, by Chapman and Bonness, to produce the experimental curve shown in Figure 10. The trends between both curves are similar, however, discrepancies do exist between both sets of data. As shown earlier, the predicted pressure coefficients of the unfinned, two body case were shown to agree well with experimental data. The relative difference between the experimental interference force and the predicted force appears large, but the absolute difference is consistent with the absolute differences in C_p . Calculation of the interference force from ΔC_p for this body of revolution results in small forces and a magnification of the relative difference. This is true for both the experimental and computational approaches. The predicted value of interference force at each freestream Mach number is within the measure uncertainty of the experimental data. The absolute difference in the forces is small, and for a finned body with larger forces, the absolute difference should be comparable to that seen here, assuming the flowfield is predicted with the same accuracy.

In comparing the computed interference force to lift forces computed from experimental data, it is found that the interference forces computed here fall within the range of the lift experienced by a single body at angles of attack varying between 4° and 10° . This estimate should only be viewed as an approximate one in view of the discrepancies observed in Figure 10.

The three store mesh described above was used to run a single case of three body interference. The flow solution was obtained for the parameters $M_\infty = 0.95$ and $D = 1.6$ inches. The addition of a third body increases the flow interference level in comparison to the two body problem. The attractive force towards the axis of the three body configuration was, $C_A = 0.092$. This represents a 65% increase in comparison to the two body problem. Further investigations of three body interference are planned.

CONCLUSIONS

Flow solutions were computed, using a thin-layer, Navier-Stokes solver, about interfering bodies. The computed pressure distributions along the body com-

pared well with available experimental data at a separation distance of 1.6 inches.

Three regions along the body which contribute to repulsive interference forces and two regions which contribute to attractive interference forces were identified. The combined effects of these regions determine the total interference force. For all cases investigated here, that force was an attractive force. It increases with free stream Mach number at the lower range of Mach numbers considered, and decreases with free stream Mach number at the higher range of Mach numbers considered. At a given free stream Mach number value, the interference force was found to increase as the separation distance decreases.

Flow interference measured by the deviation from symmetry between the inboard and outboard pressure distributions along the body surface show that the level of interference, in general, increases with free stream Mach number and decreases with separation distance. However, at the upper range of Mach numbers considered, the increase of flow interference with free stream Mach number becomes small for the large separation distance. For the small separation distance, a slight reduction in interference with increased Mach number is observed at the higher range of Mach numbers considered here.

REFERENCES

- [1] Cottrell, C.J., Martinez, A., and Chapman, G.T., "A Study of Multi- Body Aerodynamic Interference at Transonic Mach Numbers", AIAA-87-0519. In *AIAA 25th Aerospace Sciences Meeting*, Reno, 1987.
- [2] Lijewski, L.L., "Transonic Euler Solutions on Mutually Interfering Finned Bodies", In *AIAA Journal*, Volume 28, Number 6, pp. 982-988, June 1990.
- [3] Thompson, J.F., and Gatlin, B., "Program EAGLE User's Manual, Vol I and II, Surface and Grid Generation Codes," AFATL-TR-88-117, September 1988.
- [4] Simpson, L.B., and Whitfield, D.L., "A Flux-Difference Split Algorithm for Unsteady Thin-Layer Navier-Stokes Solutions", AIAA-89-1995. In *AIAA 9th Computational Fluid Dynamics Conference*, Buffalo, 1989.
- [5] Cottrell, C.J., and Martinez, A., "Experimental and Numerical Data for Transonic Mutual Interference Around Unfinned Bodies", AFATL-TR-86-75, October 1986.

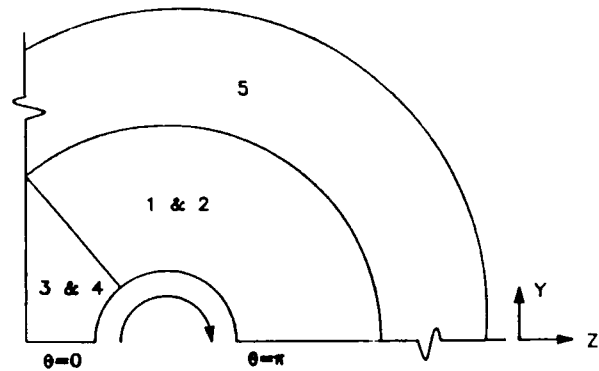


Figure 1(a). Cross-Sectional View of Two Store Grid

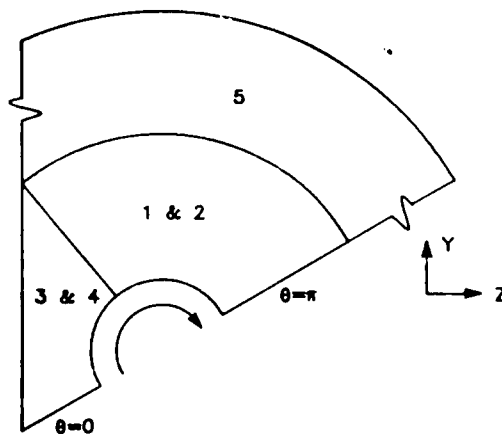


Figure 1(b). Cross-Sectional View of Three Store Grid

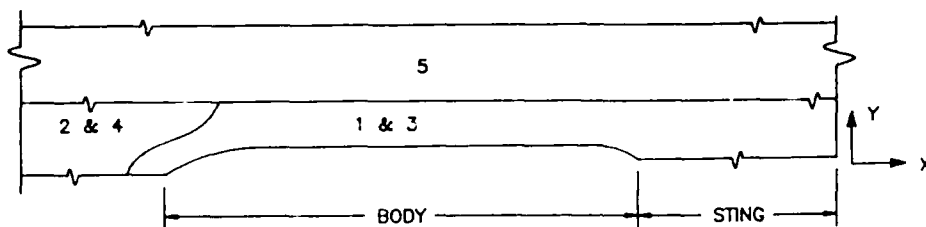


Figure 1(c). Lengthwise Sectional View of Two and Three Store Grid

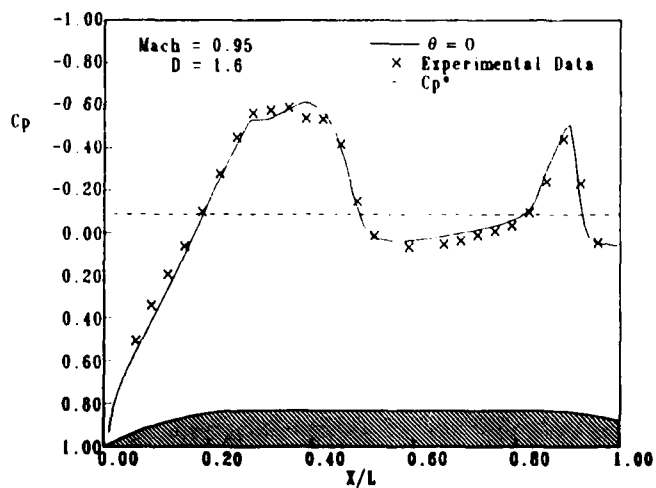


Figure 2(a). Computational versus Experimental Pressure Distribution, Two Body Case

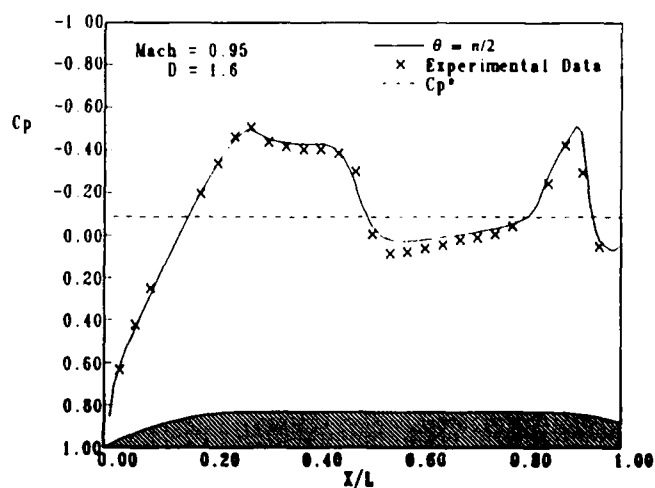


Figure 2(b). Computational versus Experimental Pressure Distribution, Two Body Case

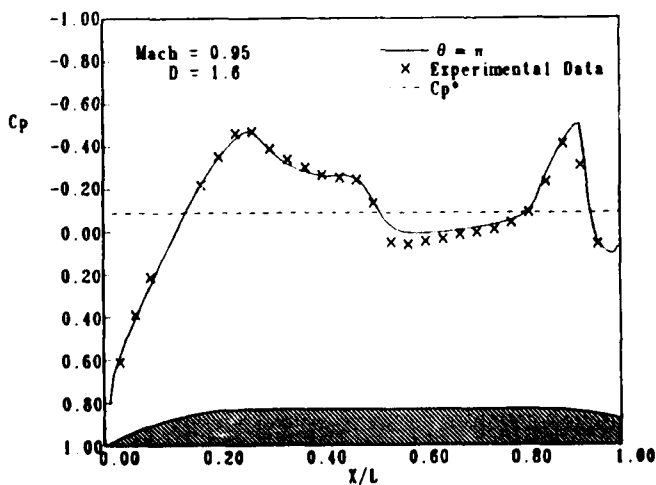


Figure 2(c). Computational versus Experimental Pressure Distribution, Two Body Case

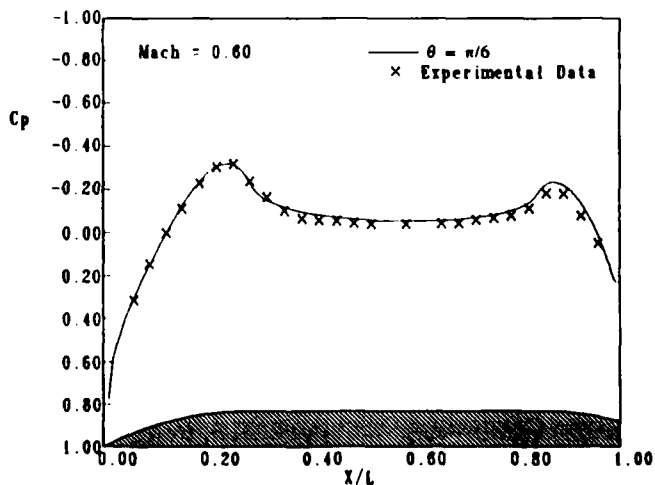


Figure 3(a). Computational versus Experimental Pressure Distribution, Two Body Case

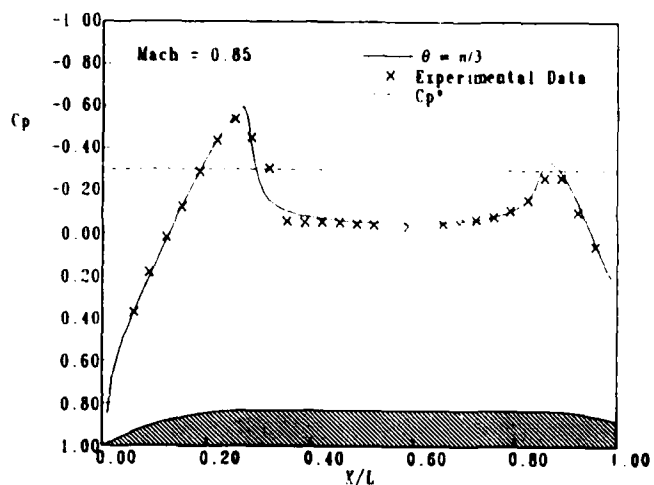


Figure 3(b). Computational versus Experimental Pressure Distribution, Two Body Case

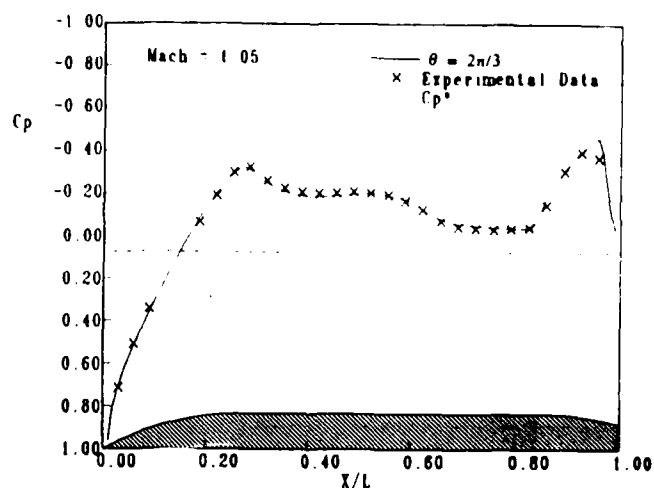


Figure 3(c). Computational versus Experimental Pressure Distribution, Two Body Case

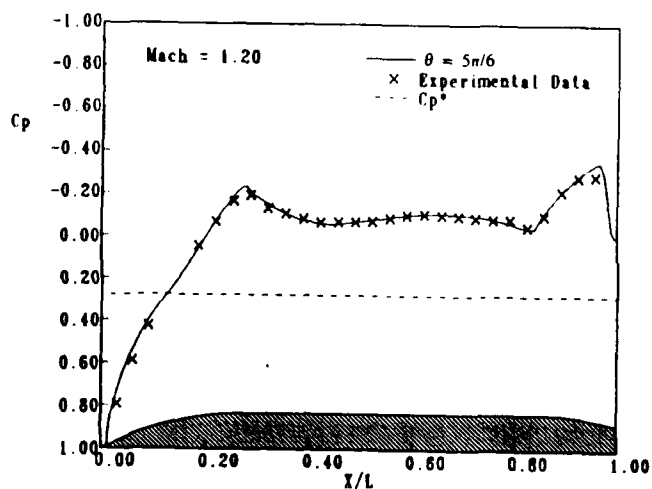


Figure 3(d). Computational versus Experimental Pressure Distribution, Two Body Case

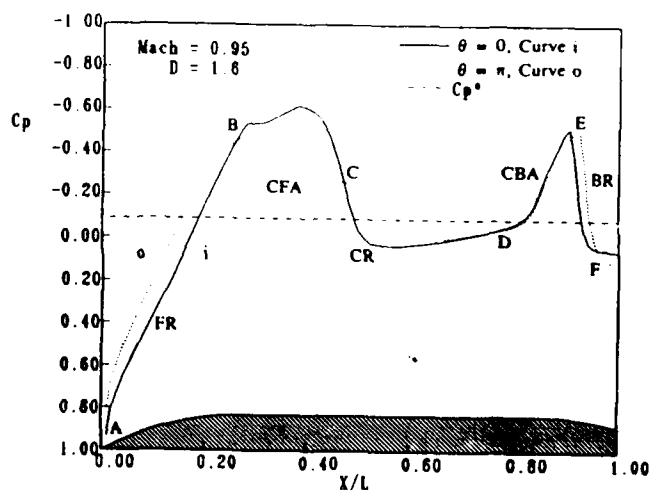


Figure 4(a). Comparison of Pressure Distributions Showing Interference Force Regions

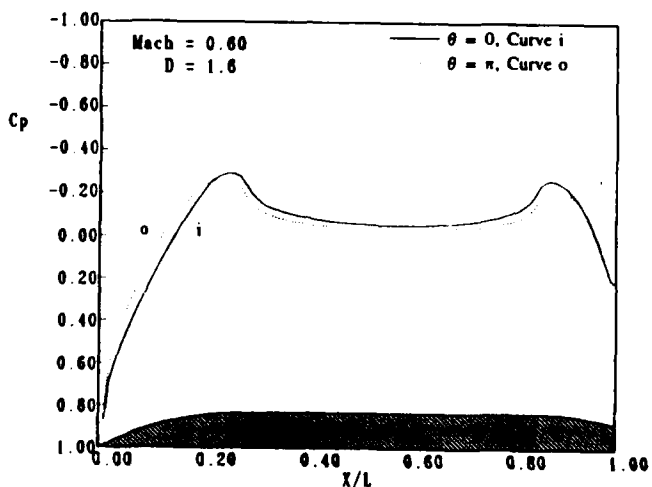


Figure 4(b). Aerodynamic Interference Comparisons

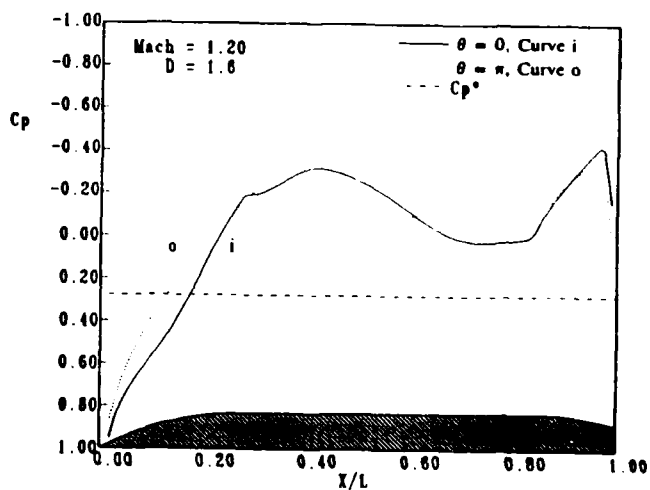


Figure 4(c). Aerodynamic Interference Comparisons

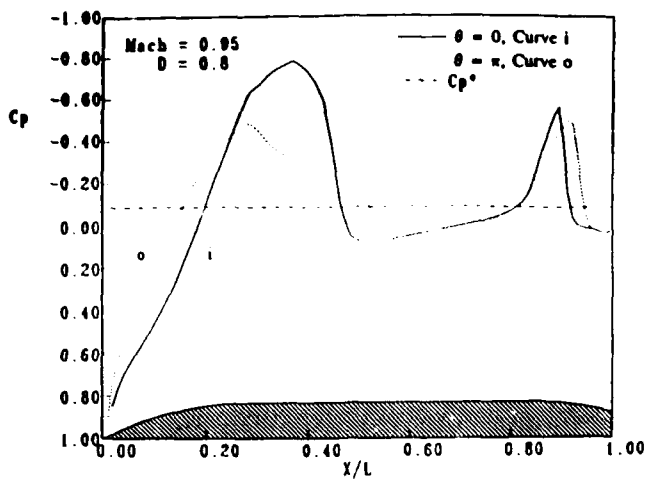


Figure 5(a). Aerodynamic Interference Comparisons

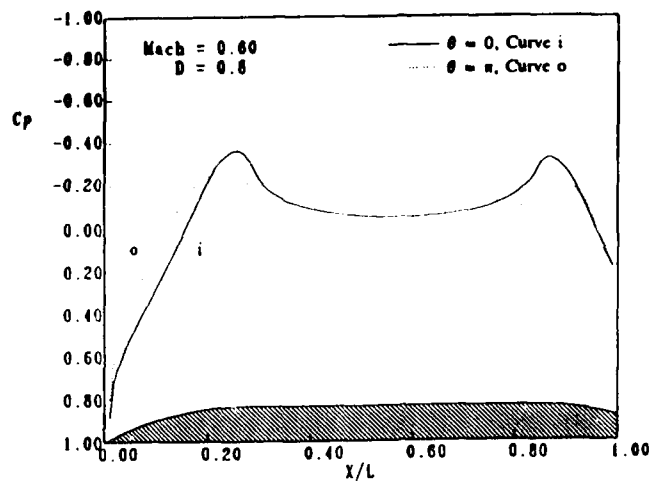


Figure 5(b). Aerodynamic Interference Comparisons

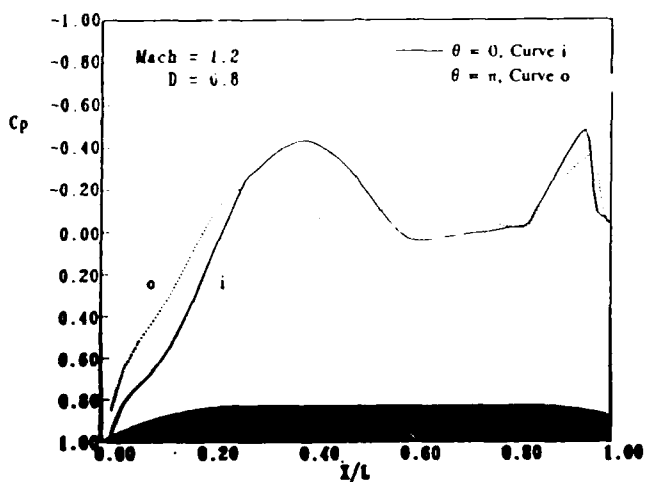


Figure 5(c). Aerodynamic Interference Comparisons

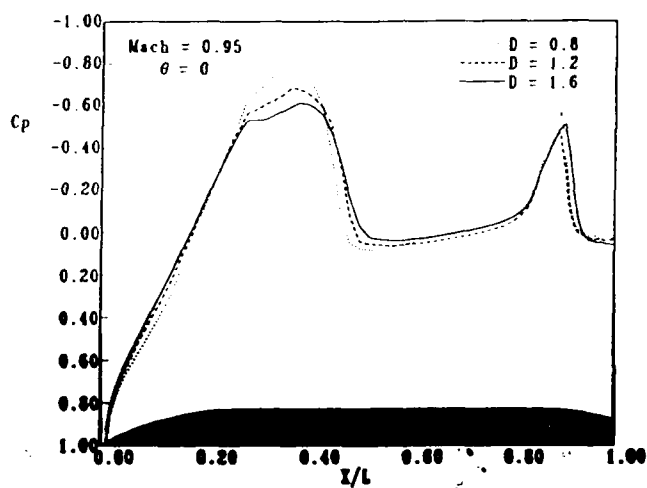


Figure 6(a). Variation of C_p with Increasing Separation Distance, D

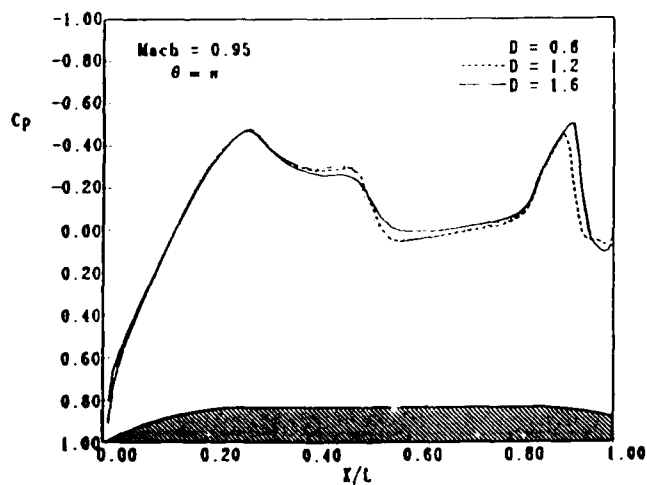


Figure 6(b). Variation of C_p with Increasing Separation Distance, D

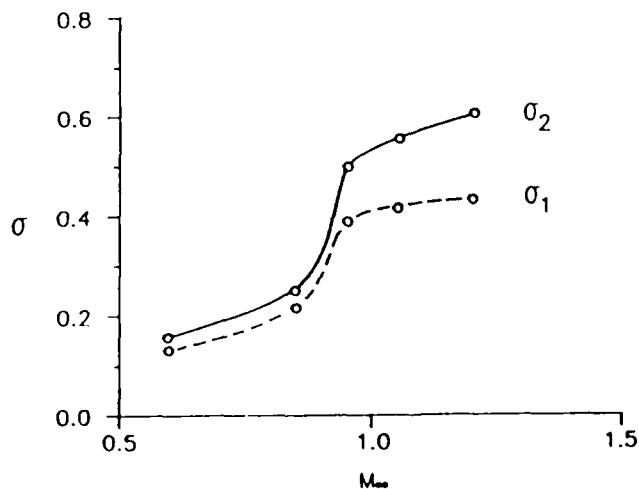


Figure 7. M_∞ Effect on Interference Parameters, $D = 1.6$ Inches

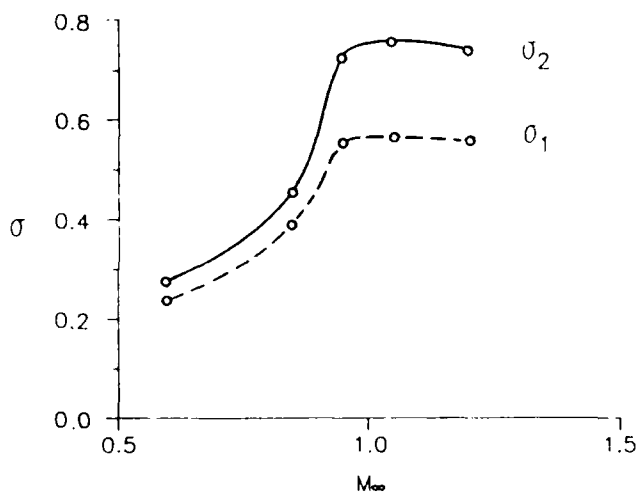


Figure 8. M_∞ Effect on Interference Parameters, $D = 0.8$ Inches

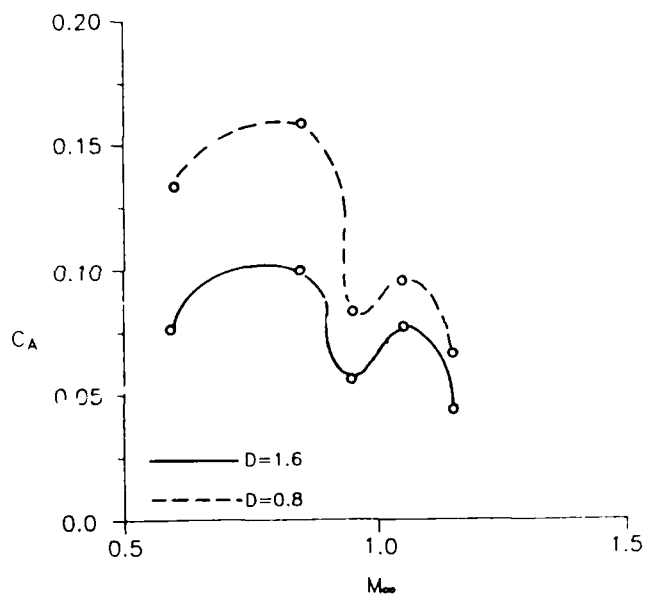


Figure 9. Effects of M_∞ and D on Interference Force

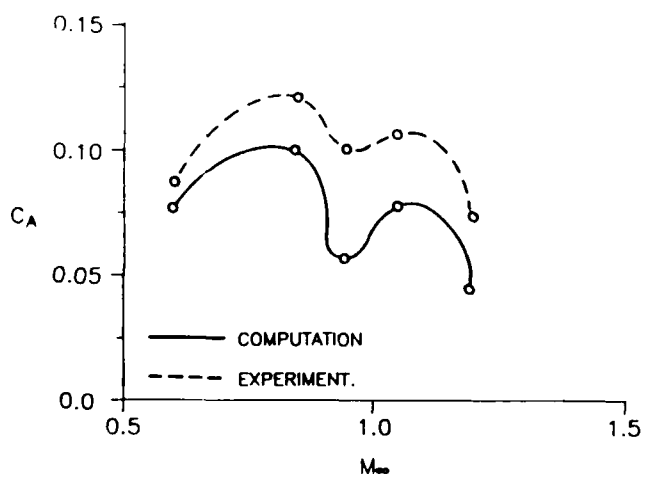


Figure 10. Comparison of Computational and Experimental Interference Force, $D = 1.6$ Inches